2016

Stereo-PIV Measurements of Vapor-Induced Flow Modifications in Confined Jet Impingement Boiling

M. J. Rau
Purdue University

T. Guo

P. P. Vlachos

S V. Garimella
Purdue University, sureshg@purdue.edu

Rau, M. J.; Guo, T.; Vlachos, P. P.; and Garimella, S V., "Stereo-PIV Measurements of Vapor-Induced Flow Modifications in Confined Jet Impingement Boiling" (2016). *CTRC Research Publications.* Paper 304.
http://dx.doi.org/http://dx.doi.org/10.1016/j.ijmultiphaseflow.2016.03.006

Stereo-PIV Measurements of Vapor-Induced Flow Modifications in Confined Jet Impingement Boiling[1]

Matthew J. Rau, Tianqi Guo, Pavlos P. Vlachos, Suresh V. Garimella[2]

School of Mechanical Engineering, Purdue University, 585 Purdue Mall, West Lafayette, IN 47907 USA

Abstract

A single subcooled jet of water which undergoes boiling upon impingement on a discrete heat source is studied experimentally using time-resolved stereo particle image velocimetry (PIV). The impinging jet issues from a 3.75 mm diameter sharp-edged orifice in a confining orifice plate positioned 4 orifice diameters from the target surface. The behavior at jet Reynolds numbers of 5,000 and 15,000 is compared for a constant jet inlet subcooling of 10 °C. Fluorescent illumination allows for simultaneous imaging of both the flow tracers and the vapor bubbles in the flow. Flow structure, time-averaged velocities, and turbulence statistics are reported for the liquid regions within the confinement gap for a range of heat inputs at both Reynolds numbers, and the effect of the vapor generation on the flow is discussed. Vapor generation from boiling is found to modify the liquid velocities and turbulence fluctuations in the confinement gap to a significant extent. Flow in the confinement gap is dominated by vapor flow, and the vapor bubbles disrupt both the vertical impinging jet and horizontal wall jet flow. Moreover, vapor bubbles are a significant source of turbulence kinetic energy and dissipation, with the bubbly regions above the heated surface experiencing the most intense turbulence modification. Spectral analysis indicates that a Strouhal number of 0.023 is characteristic of the interaction between bubbles and turbulent liquid jets.

[1] Submitted for consideration in *International Journal of Multiphase Flow*, December 2015
[2] Corresponding author, Tel: +1 765 494 5621. E-mail address: sureshg@purdue.edu

Keywords

jet impingement, boiling, two-phase flow, turbulence, PIV, fluorescent imaging

1. Introduction

Impinging jets are commonly used in applications requiring high convective heat transfer coefficients such as turbine-blade cooling, heat treating of metals, glass tempering, and thermal management of electronics devices. Recent interest in two-phase jet impingement has been driven by the need to effectively cool high-power electronics devices at reduced pumping power relative to traditional single-phase liquid cooling loops. Boiling can greatly augment the cooling capabilities of impinging jets, resulting in higher heat transfer coefficients and increased surface temperature uniformity compared to single-phase impingement (Wolf *et al.* 1993; Rau and Garimella 2013; Qiu *et al.* 2015).

Recent two-phase jet impingement studies demonstrated a four-fold enhancement of critical heat flux (CHF) with minimal increases in pressure drop, achieved by tailoring surface enhancement structures to the impingement geometries (Rau and Garimella 2014; Rau *et al.* 2015). A pressure drop increase of only 0.6 kPa compared to single-phase operation was observed even when the vapor mass fraction at the heat sink outlet reached 54%. Conventional flow boiling in straight channels, in contrast, suffers from much greater increases in pressure drop relative to single-phase flow; the promising results from these jet impingement studies have therefore motivated further study of the flow physics in two-phase jet impingement.

The flow characteristics of single-phase impinging jets have been studied in great detail in the literature. Initially motivated by vertical take-off and landing applications (Bradshaw and Love 1959) for thrust generation, interest has more recently focused on the large heat and mass transfer coefficients achieved by impinging jets (Donaldson *et al.* 1971; Martin 1977; Popiel and Trass 1991; Cornaro *et al.* 1999). Confined impinging jets have received special attention (Fitzgerald and Garimella 1997, 1998; Morris and Garimella 1998; Garimella 2000) in view of their applicability to electronics cooling. Confinement allows impingement cooling technologies to be integrated into more compact electronics

packages compared to unconfined geometries. The authors are not aware of any existing study that directly measures the flow field in an impinging jet during boiling. Vader *et al.* (1992) showed that the transition to turbulence in a developing wall jet issuing from a free impinging slot jet is strongly affected by the point at which the onset of nucleate boiling (ONB) occurs. Their conclusions were indirectly deduced from measurements of the local wall temperature and qualitative flow visualizations.

Boiling causes modifications to both time-averaged flow velocities and turbulence characteristics (Estrada-Perez and Hassan 2010; Hassan *et al.* 2014). Turbulence is particularly of interest because it affects flow regime development (Balachandar and Eaton 2010). Experiments are usually relied upon to characterize and understand the complex interactions between vapor bubbles and turbulent liquid flows. The measurements performed by Roy *et al.* (1993) of liquid turbulence adjacent to the bubbly boundary layer in their annular flow boiling experiment showed that velocity fluctuations outside the bubbly region increased as a result of the vapor formation occurring in the adjacent boundary layer. In an extension of this study, Roy *et al.* (1997) used laser Doppler velocimetry (LDV) to include liquid velocity measurements within the bubbly boundary layer close to the inner heated wall. The production of turbulence kinetic energy close to the wall increased due to high Reynolds shear stresses in these regions induced by boiling. Estrada-Perez and Hassan (2010) used particle tracking velocimetry (PTV) to report turbulent statistics for subcooled flow boiling through a vertical rectangular channel with one heated wall. They showed that increasing vapor generation increased the mean and fluctuating liquid velocities, primarily in the near-wall region. This effect of heat flux decreased with increasing Reynolds number.

Vapor bubbles can have a large effect on a turbulent liquid flow field, but there is a significant gap in the understanding of the flow physics in confined two-phase jet impingement. In the present study, the flow characteristics of confined jet impingement during subcooled boiling from a discrete heat source are studied experimentally using time-resolved stereo particle image velocimetry (PIV). The mean and fluctuating velocities throughout the confinement gap are reported as a function of heat flux at jet Reynolds numbers of 5,000 and 15,000. Spatial distributions of turbulent kinetic energy and turbulent

kinetic energy dissipation rate are also presented and the effects of vapor bubbles on turbulence in the flow field are discussed.

2. Experimental Facility

The flow loop constructed for this study is shown schematically in Figure 1. A magnetically coupled gear pump circulates deionized water through the loop and a metering valve is used to finely tune the rate of flow entering the test section. A Coriolis flow meter (CMFS015M, Emerson) measures the mass flow rate with a measurement uncertainty of ± 0.1%. The inline liquid preheater is adjusted to maintain a jet inlet subcooling of 10 °C in the test section. After exiting the test section, the water passes through a liquid-to-air heat exchanger to condense any vapor and cool the flow before it enters the reservoir. A custom-manufactured expandable reservoir allows flow loop pressure control; the volume can be expanded to relieve pressure rise due to fluid heating and vapor generation to maintain a constant pressure in the test section. For degassing, the reservoir also includes two reflux condensers and a 1 kW immersion heater.

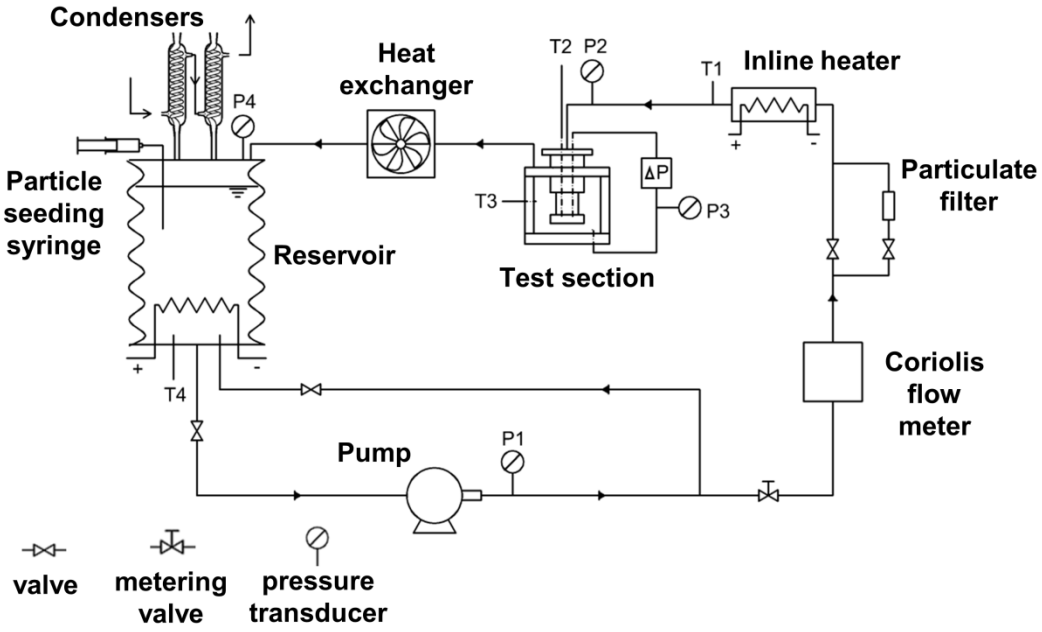

Figure 1. Schematic diagram of the experimental flow loop.

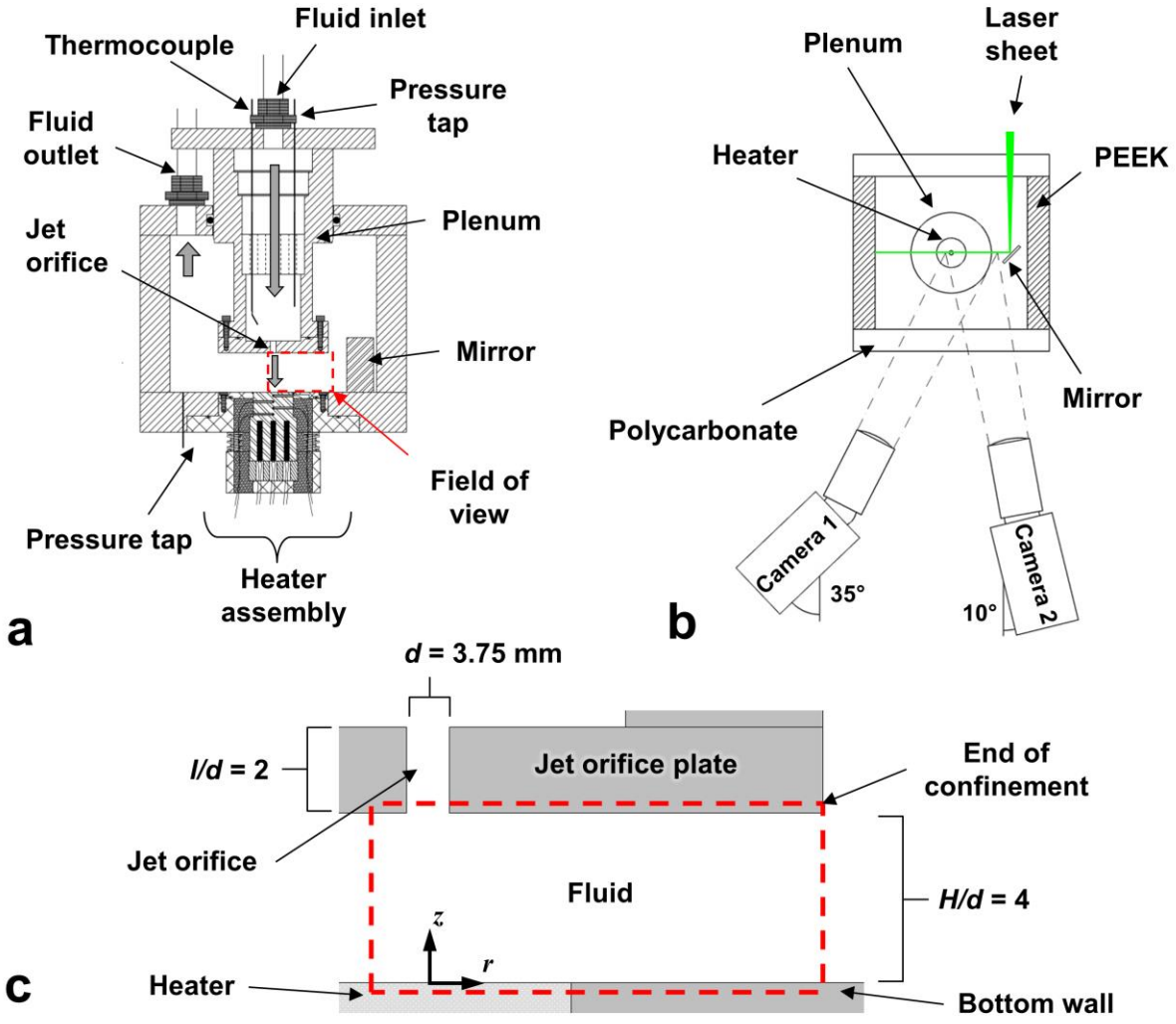

Figure 2. (a) Front-view cross-sectional diagram of the confined jet impingement test section, (b) top-view cross-sectional diagram of the test section showing the orientation of the laser light sheet and stereo-PIV cameras, and (c) to-scale diagram of the field of view of the cameras showing the relative locations of the jet orifice, confinement plate, and heat source.

A schematic diagram of the test section is shown in Figure 2, along with the orientation of the PIV cameras. The test section is adapted from previous studies by the authors (Rau and Garimella 2013, 2014; Rau *et al.* 2015). Only relevant details of the test section are described here for brevity, and additional information can be found in these references. The test section is fabricated from polyether ether ketone (PEEK) with polycarbonate front and back walls to allow visualization of the flow. Water flows into the jet plenum and is conditioned by two screens and a flow-straightening honeycomb before

entering a sharp-edged orifice to form the impinging jet. The orifice has a diameter (d) of 3.75 mm, is two diameters long (l/d = 2), and is machined into the center of a jet orifice plate. The jet orifice plate is mounted and sealed to the end of the plenum and has a diameter (D) of 70 mm. The confinement gap is created between the test section bottom wall and upper confining orifice plate as shown in the to-scale drawing in Figure 2c. For the present geometry, the confinement gap extends to 9.3 jet diameters radially from the jet axis. The confinement-gap height is maintained at 4 jet diameters (H/d = 4) by resting the jet orifice plate on precision-machined spacers.

A circular copper heat source is installed in the test section for this two-phase flow study and is shown in cross-section in Figure 1a. This heating block is powered by twelve 100 W embedded cartridge heaters and is insulated and sealed at its upper edge with a small bead of silicone sealant as described in Rau and Garimella (2014). The sealant is applied in a 1 mm-wide chamfer groove machined into the PEEK insulation that surrounds the upper edge of the heat source. The resulting exposed (*i.e.* wetted) area of the planar heat source is 25.4 mm in diameter. The size of the heat source is chosen to approximate a typical power electronics device; the circular shape is chosen to maintain axisymmetric boundary conditions. The copper heating block is plated with 5 μm of nickel (Ni) and 1 μm of gold (Au) to prevent oxidation.

The surface temperature of the heating block is extrapolated from the vertical centerline temperature gradient, as measured by four T-type thermocouples positioned at 4 mm intervals. The jet inlet temperature is measured with a T-type thermocouple located just upstream of the jet orifice plate. The uncertainty in thermocouple measurements is estimated based on the calibration at ± 0.3 °C; the extrapolation used to calculate surface temperature results in a higher uncertainty (a maximum of 1 °C at the highest heat flux reached in this study of 137 W/cm^2). The heat flux into the fluid is calculated from the total electrical heat input by subtracting the estimated heat lost by conduction, based on a heat loss analysis performed in FLUENT as described in Rau and Garimella (2014). Uncertainty in heat flux is estimated to be ± 2% based on the temperature and power measurements used for the heat flux

calculation. The water saturation temperature is calculated based on the pressure inside the test section measured using a pressure transducer with a 0 to 103 kPa range and calibrated uncertainty of ± 0.13 kPa.

3. Experimental Methods

3.1. PIV measurements

Flow measurements are obtained using a time-resolved stereo-PIV system. A high-speed Nd:YLF laser (Terra PIV, Continuum) delivers two pulses of 527 nm light at a rate of 750 Hz. The laser beam is formed into a 2 mm-thick light sheet with a beam collimator and two cylindrical lenses. A mirror (83-536, Edmund Optics) mounted directly on the test section bottom wall reflects the light sheet across the axisymmetric plane of the confinement gap, as shown in Figure 2b.

Single-exposure PIV images are acquired at a resolution of 1104 × 1600 pixels with two high-speed cameras (Phantom Miro M340, Vision Research) mounted on a common side of the test section. The imaging axes of the cameras are parallel to the test section bottom wall, and the cameras view the experiment through Scheimpflug lens-tilt adapters (Prasad and Jensen 1995) and macro lenses (Makro-Planar T* 2/100, Carl Zeiss). The resulting field-of-view (FOV) of the jet and right side of the confinement gap is shown in Figure 2c.

Spherical polystyrene particles, 10 μm in diameter, are used as flow tracers. The particles (Spherotech) have a density of 1.05 g/cm^3 and are fluorescent with a peak emission wavelength of approximately 560 nm, allowing the reflected laser light (λ = 527 nm) to be optically filtered from the images using long-pass optical filters (FELH0550, Thor Labs). Fluorescent particle imaging is necessary to obtain clean particle images in close proximity to vapor bubbles (Hassan *et al*. 1992).

PEEK (the primary material used to build the test section) was found to emit orange light (λ > 550 nm) when excited with a green laser. The combined emitted light from the fluorescent particles and PEEK walls yielded very clear illumination of both the particles and vapor structures in the experimental images, as shown later in Figure 5. No additional lighting or shadowgraphy is needed for detection of the gas phase in the raw experimental images.

3.2. Stereo-camera calibration

Prior to experimentation, the cameras are calibrated using a single-level dot-matrix target with 0.5 mm-diameter dots spaced 1.0 mm apart (FA131, Max Levy Autograph). The calibration target is hung inside the test section chamber from a micrometer stage, with the jet plenum and test section top removed. The test section is filled with water so that the resulting coordinate-mapping functions incorporate the refractive index variations along the viewing path that are present during experimentation (*i.e.* the air–polycarbonate interface and polycarbonate–water interface). The calibration target is translated from -1.5 mm to +1.5 mm in the out-of-plane direction and calibration images of the target are acquired at 0.5 mm increments. A polynomial (3^{rd} order in r and z, 2^{nd} order in the out-of-plane direction) is then fit to the detected dot positions (Soloff *et al.* 1997). A self-calibration step to correct for misalignments in the calibration procedure is also performed as described by Wieneke (2005).

3.3. Test procedure and data acquisition

Water in the flow loop is degassed by circulating it at a flow rate of 600 ml/min while causing it to boil with both the immersion heater in the reservoir and the inline heater turned on, and the heat exchanger fan turned off. The reservoir is expanded to allow a vapor gap at the top of the reservoir and noncondensable gas is vented to the ambient atmosphere through the Graham reflux condensers. After 2 hr of degassing, the reservoir volume is compressed to eliminate the vapor gap and sealed from the atmosphere to create a closed system.

The water flow rate and power to the immersion and inline heaters are adjusted to maintain the jet at the desired Reynolds number with an inlet subcooling of 10 °C. Water properties are determined based on the jet temperature. Power to the heater block is incrementally raised to perform a boiling experiment; 2 min of steady-state data (sampled at 1 Hz) are collected at each power increment. PIV images are acquired at the end of this data acquisition period. Flow tracers are added in the reservoir so that the

injection of particles has a minimal effect on the steady conditions in the test section. PIV images are recorded continually for 3 seconds, corresponding to 2250 time-resolved image pairs.

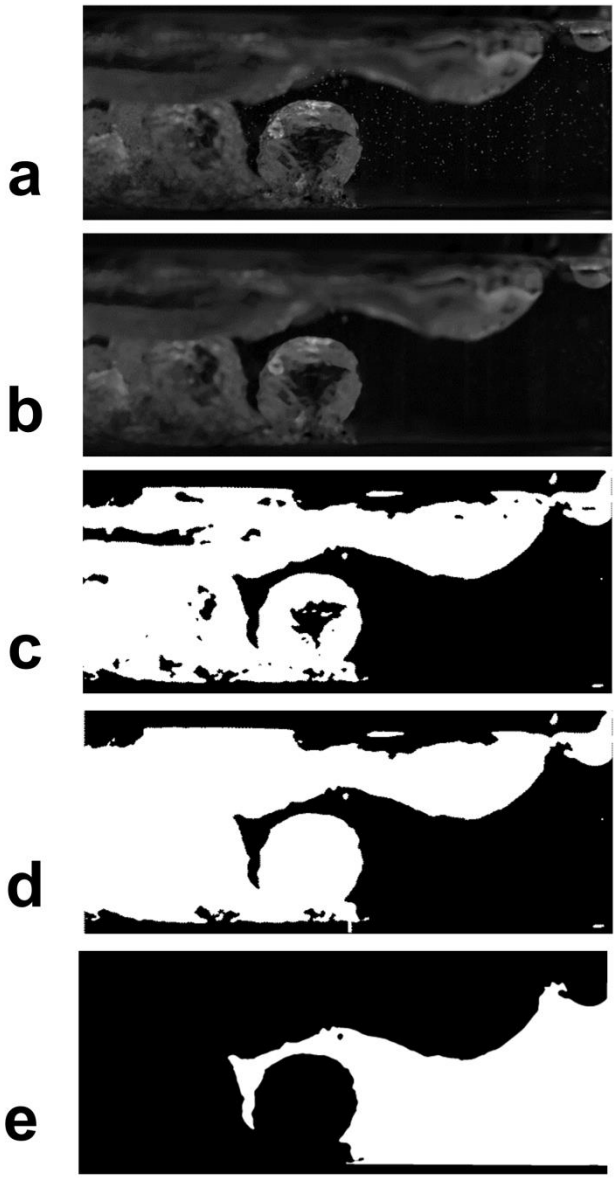

Figure 3. Image processing steps used to create vapor masks for PIV evaluation: (a) raw image, (b) median-filtered image, (c) image after thresholding, (d) image after filling of holes, and (e) final vapor-phase mask.

3.4. Data reduction

3.4.1. Image pre-processing and masking

To separate the measurement signals for each respective phase, visualization-based measurement techniques such as PIV require phase detection in the experimental images. Concurrent shadowgraph experiments have often been used to obtain high-contrast images of the dispersed phase (Hassan *et al*. 2014; Lindken and Merzkirch 2002). In the current experiments, concurrent shadowgraphy is unnecessary as the vapor phase is clearly illuminated in the raw images (shown in Figure 5) and can be readily detected using an image processing method.

Various methods have been proposed in the literature to automatically detect vapor regions and boundaries in images (Khalitov and Longmire 2002). A size-based discrimination method is chosen for the current study due to the large differences observed between typical particle image size (3-5 pixels) and vapor bubble image size (> 100 pixels).

A set of dynamic masks is created for each camera. The background intensity from the raw images is first removed by subtracting the minimum gray-level intensity at each pixel as calculated from the entire set of 2250 images. The subsequent steps for dynamic vapor mask creation are explained below with example results at key steps shown for camera 2 in Figure 3.

- A median filter is applied with a 12 × 12 pixel kernel resulting in the image in Figure 3b.
- The local minimum, calculated over a 25 × 25 pixel kernel, is subtracted at each pixel.
- A gray-level threshold is calculated using a fuzzy c-means clustering technique (Xiong *et al*. 2006). The image is then binarized based on this threshold, as shown in Figure 3c.
- Regions surrounded by a value of 1 are assigned a value of 1, as shown in Figure 3d.
- Any object larger than 100 pixels is assumed to be a vapor bubble. Smaller objects, such as particles, are discarded.
- The binary values are inverted and combined with a static mask of the wall regions. The final mask, which includes both the vapor and wall regions, is shown in Figure 3e.

The above steps may be automated for most images. Low-intensity vapor illumination occasionally causes regions to be improperly masked; these areas are then masked manually. Small areas of liquid in close proximity to vapor structures are occasionally masked by the above algorithm, which results in a conservative estimate of the liquid regions for PIV evaluation. Only the regions overlapping in both camera masks contribute to the final reported velocity fields.

3.4.2. PIV processing

In-house codes are used for PIV processing. Image pairs from each camera are cross-correlated separately and the v_r-, v_z-, and v_θ-component velocities are reconstructed using the method described in Soloff *et al*. (1997). A multipass scheme using a robust phase correlation (Eckstein *et al*. 2008; Eckstein and Vlachos 2009a; 2009b) is applied with 48 × 48 ($r \times z$) pixel windows on the first pass and reduced to 48 × 32 pixel windows in subsequent passes. A 75% window overlap results in a final measurement resolution of 0.29 × 0.19 mm (12 × 8 pixels) in all regions defined as liquid by the dynamic masks described in Section 3.4.1. Universal outlier detection (Westerweel and Scarano 2005) is used for vector validation between passes and after the 3rd and final pass. To resolve the thin boundary layer of the time-averaged single-phase wall jet, an ensemble correlation with windows of 64 × 8 pixels are used on the final pass to increase the measurement resolution in the z-direction to 0.05 mm.

The mean velocity is obtained by time-averaging the instantaneous velocity over the entire data sample length available at a given position. The velocity fluctuations are obtained through a standard Reynolds decomposition: for example, for the v_r-component, $v_r'(t) = v_r(t) - \bar{v}_r$, where $v_r'(t)$ is the instantaneous radial velocity fluctuation, $v_r(t)$ is the instantaneous radial velocity, and $\bar{v}_r$ is the time-averaged radial velocity.

The convergence of the velocity statistics must be carefully considered (Estrada-Perez and Hassan 2010; So *et al*. 2002). At any given time instant, vapor bubbles can intercede and obscure the view of the liquid from either camera, effectively reducing the liquid velocity data sampling length at a given position

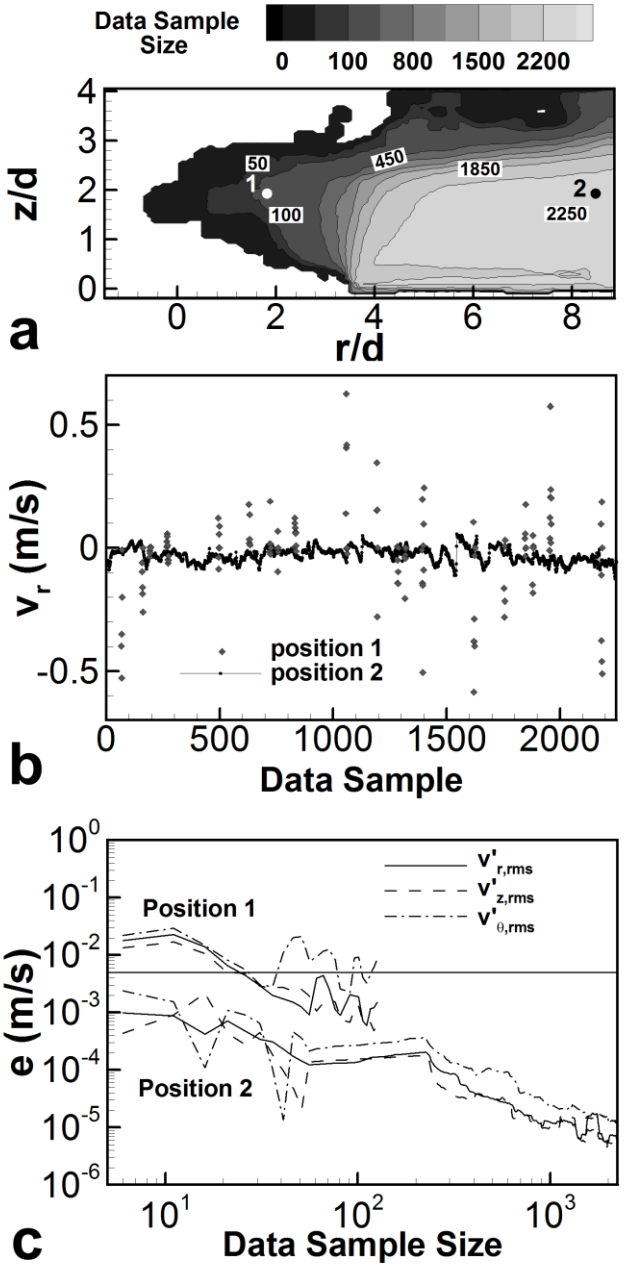

Figure 4. (a) A contour plot of the data sample size available throughout the field of view for *Bl** = 1.34, Re = 5,000 as an example data set, and (b) radial velocity sampling at the two positions labeled in (a). The change in rms velocity fluctuations (*e*) with increasing data sample length for (c) Position 1 and (d) Position 2.

in the FOV. As an example, the spatial distribution of data sample length available in a case with a large amount of vapor generation is shown in Figure 4a, with the instantaneous radial velocity signals at 2 locations shown in Figure 4b. The intermittent velocity sampling at Point 1 is characterized by sparse

measurement (only 128 velocity samples) of the highly fluctuating velocity at this location. Point 2 shows a low-velocity region with no vapor; the full data sample length of 2250 velocity measurements is available at this location. To determine which locations to retain for further analysis, a criterion is implemented: Locations which yield fewer than 50 data samples (50 data samples corresponds to the 60 ms periodicity observed for vapor bubble departure) are first excluded from the analysis. The statistical convergence at the remaining locations is then evaluated by calculating the change in statistical quantity (*e*) with increasing sample length, as given for the $v'_{r,rms}$ velocity by

$$e = \sqrt{\frac{1}{n}\sum_{i=1}^{n} v'^{2}_{r,i}} - \sqrt{\frac{1}{n-1}\sum_{i=1}^{n-1} v'^{2}_{r,i}}\,, \tag{1}$$

where *n* is the current data sample. Convergence is satisfied when the change in time-averaged *and* rms fluctuations of each velocity component are lower than 0.005 m/s, which is representative of the measurement uncertainty for the current experiments, estimated based on the primary-peak ratio method of Xue *et al*. (2015). In the examples shown in Figure 4, Point 1 is discarded as all rms velocity components do not satisfy the convergence criterion, as shown in Figure 4c, while Point 2 is retained for further analysis.

3.4.3. Non-dimensionalization

A comparison at different heat fluxes across different mass flow rates necessitates non-dimensionalization due to the dependence of flow boiling on liquid inlet mass flow rate and subcooling. Comparisons in the rest of this work are made with a non-dimensional heat input (*Bl**), given as

$$Bl^{*} = \frac{q}{\dot{m} c_p \left(T_{sat} - T_j\right)}, \tag{2}$$

where q is the heat input, $\dot{m}$ the mass flow rate, c_p the specific heat of water, T_{sat} the saturation temperature, and T_j the jet temperature. The denominator represents the heat input necessary to reach saturated conditions based on an energy balance. This non-dimensional number is similar in concept to

the Boiling number $\left(Bl = q/\dot{m}h_{fg}\right)$, which normalizes heat flux based on a maximum theoretical heat input assuming complete liquid evaporation, where h_{fg} is the latent heat of vaporization.

Turbulence intensity has been normalized in a variety of ways in the literature, including with the local centerline jet velocity (Hussein *et al*. 1994) and the friction velocity for flow boiling in a pipe (Estrada-Perez and Hassan 2010). In the present study, the local velocity and turbulence statistics are normalized based on the average jet exit velocity, which is consistent with many jet impingement studies (Fitzgerald and Garimella 1997, 1998). This normalization allows a direct comparison of the magnitude of turbulent fluctuations caused by turbulence in the liquid jet and fluctuations induced by vapor bubbles in regions away from the jet.

4. Results

The flow field characterization results at various heat inputs for Re = 5,000 and 15,000 are presented in this section. Figure 5 presents boiling curves for both Reynolds numbers, along with representative images obtained at each heat flux. A representative single-phase image with no vapor generation is also shown for comparison. The images for both Reynolds numbers show a similar qualitative evolution of vapor bubble characteristics with increasing heat flux. Just after the onset of nucleate boiling (point 1 on each curve), boiling is observed on the heated surface, though vapor generation and bubble departure are minimal due to condensation and collapse of the bubbles caused by the subcooled impinging flow.

As the heat flux is increased (point 2 on each curve), the vapor structures on the surface grow and depart from the surface resulting in a bubbly flow concentrated over the heat source. The primary flow direction for the bubbles is upwards due to buoyancy and the downward flow of the jet cannot easily be visually deduced. Further increases in heat flux (points 3 through 5 for Re = 5,000 and points 3 and 4 for Re = 15,000) cause additional coalescence of vapor with larger vapor bubbles departing from the surface, primarily near the edge of the circular heater. At the highest heat fluxes shown for both Reynolds numbers, the vapor can be characterized as a nearly continuous vapor plume above the heat source. In the

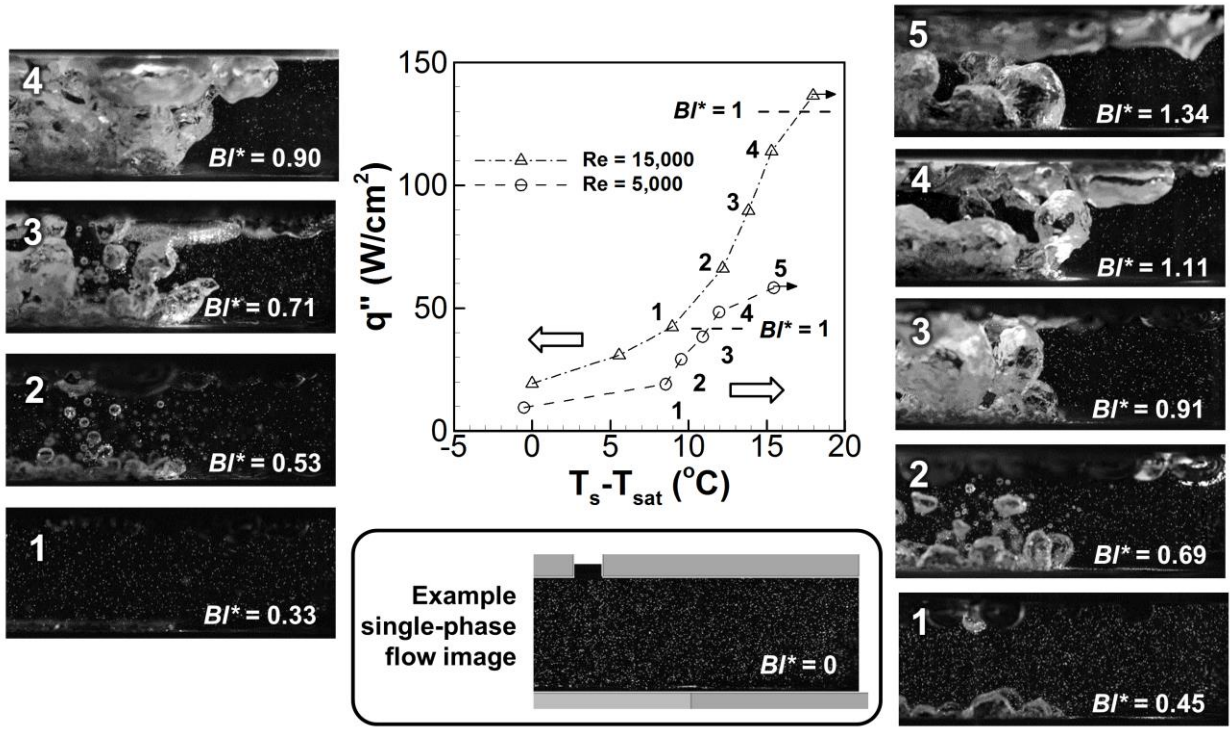

Figure 5. Boiling curves and images obtained for jet Reynolds numbers of 5,000 (right side) and 15,000 (left side). The image numbers match the numbered points on each boiling curve; they are labeled with the non-dimensional heat input. An example PIV image for the single-phase flow, with the surrounding walls shown in grey, is provided for comparison. The CHF temperature excursion is marked with a small arrow at the end of each boiling curve.

following sections, time-averaged velocities, turbulence intensities, and turbulence kinetic energy and dissipation rate for the liquid regions in these two-phase flow cases are presented, using the single-phase flow field as a baseline for comparison.

4.1. Confinement-gap flow field modification

The modification of the liquid flow pattern in the confinement gap is illustrated in Figure 6 via a comparison of the time-averaged radial velocities with increasing vapor generation resulting from increasing heat flux. The downward vertical velocity vectors centered at $r/d = 0$ also show the impinging liquid jet at those heat fluxes at which the jet is not completely obscured from view by vapor.

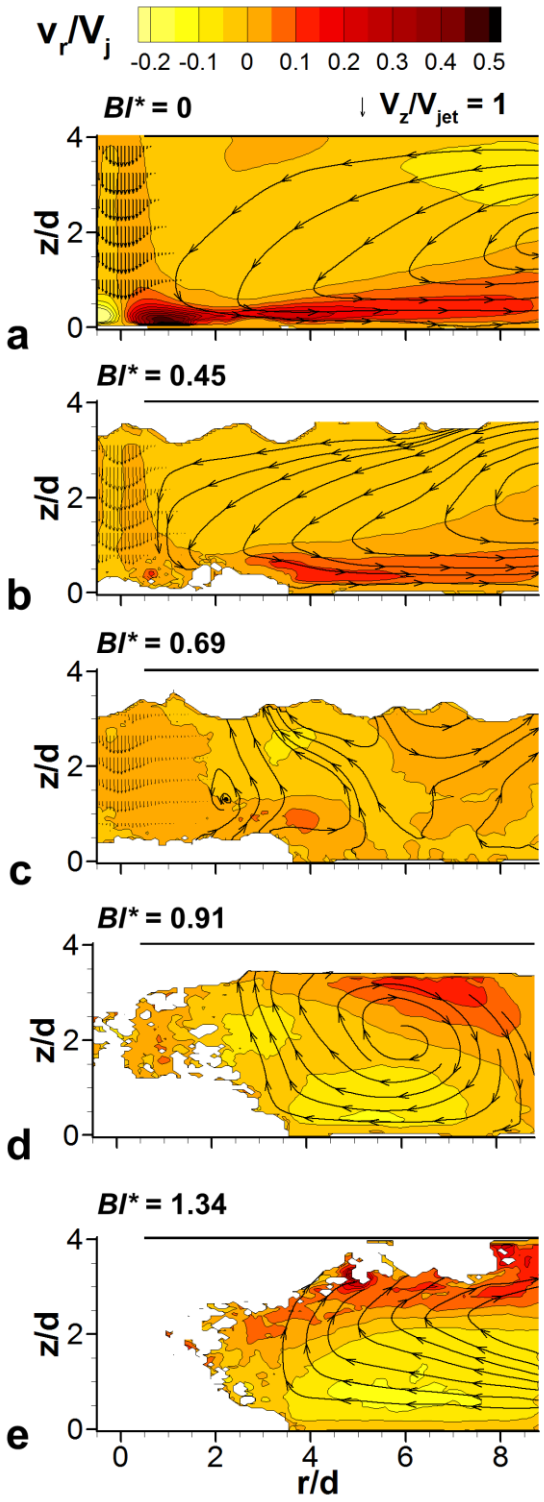

Figure 6. (a-e) Horizontal velocity contour plots with increasing heat input. The jet Reynolds number is 5,000.

The impinging jet and developing wall jet are clearly defined in the unheated single-phase flow case (Figure 6a). The wall jet, identified using the contours of radial velocity, thickens and decays in velocity magnitude as it moves radially downstream. The bulk of the flow in the confinement gap above the wall jet is characterized by a low-velocity inward flow region caused by entrainment into the impinging jet. At $Bl^* = 0.45$ (Figure 6b) measurements of liquid velocity very close to the heated surface are not possible due to the constant presence of vapor bubbles in these regions (the white areas in the figure indicate regions obscured from view or eliminated based on the convergence thresholding procedure described in Section 3.4.2). The measurements downstream of the heat source show a thicker, lower-velocity wall jet at this heat input compared to the unheated case, indicating that the radial outward flow from the impinging jet is disrupted prior to traversing past the edge of the heat source.

At a higher heat flux ($Bl^* = 0.69$ in Figure 6c), the wall jet appears to have completely vanished from the bottom wall and the resulting horizontal velocities are very low in magnitude ($v_r/V_j = 0.05$ or less). The streamtraces at $Bl^* = 0.69$ indicate that the vapor bubbles at the boiling heat source have effectively destroyed the wall jet flow and enhanced mixing; the resulting horizontal velocity profiles in the gap at this heat input are uniform and low in magnitude as shown in Figure 7. The conditions shown in Figure 6c display an important condition in the evolution of flow entrainment for confined two-phase jet impingement as it marks the end of the jet-dominated flow regime and the beginning of a vapor-dominated regime. Further increases in heat flux above $Bl^* = 0.69$ (Figure 6d,e) show a complete reversal in the confinement-gap flow pattern downstream of the heat source when compared to the unheated case (Figure 6a). These heat fluxes show a strong *inward* velocity near the bottom wall and *outward* velocity near the top wall.

Radial velocity profiles with increasing heat input are shown for both Reynolds numbers in Figure 7. The profiles at $r/d = 1$ show the high-velocity wall jet close to the bottom wall for $Bl^* = 0$. The profiles at $r/d = 5$ and 7 show the flow reversal in the confinement gap that occurs with increasing heat input. In Figure 7a for $Bl^* \geq 0.91$, the inward radial velocities near the lower wall at $r/d = 5$ and 7 are similar in magnitude to the velocities of the Re = 5,000 wall jet at $Bl^* = 0$ at this location. At a Reynolds number of

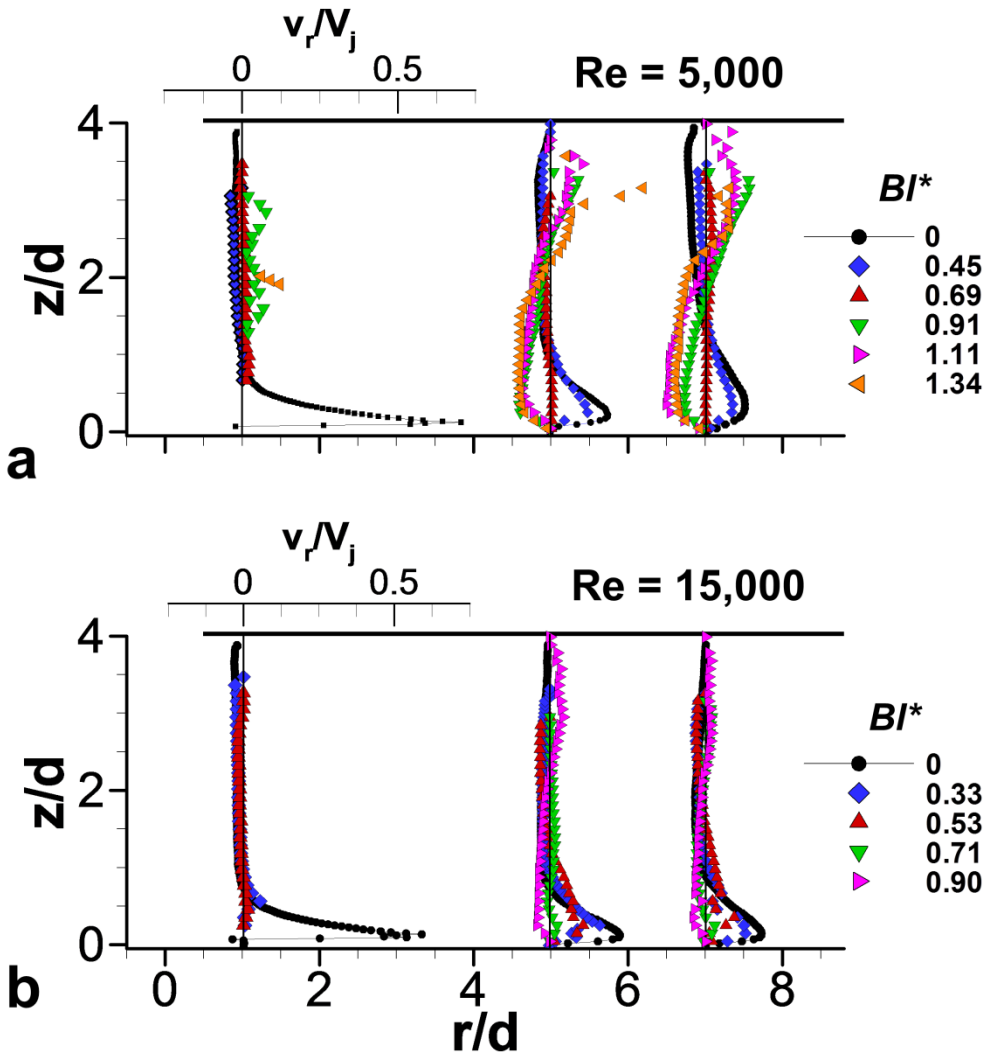

Figure 7. Horizontal velocity profiles at different radial positions as a function of heat input for the jet Reynolds number of (a) 5,000, and (b) 15,000.

15,000 (Figure 7b), the inward flow velocities at these locations for the higher heat inputs ($Bl^* \geq 0.71$) are lower in magnitude relative to the wall jet at $Bl^* = 0$. Comparing the results across jet Reynolds number indicates that the reversed flow entrainment into the confinement gap does not scale with the jet Reynolds number and is instead dominated by the vapor generation.

The destruction of the wall jet by boiling, shown in Figure 6 and Figure 7, has implications on the capability of the jet to cool the target surface. Rau and Garimella (2013) observed that the vapor film

development at CHF for single jets begins at the edges of the heat source. At low heat fluxes, the outer regions of the heat source are still exposed to the high-velocity subcooled wall jet flow. Once the wall jet is disrupted, boiling on the outer regions of the heated surface no longer benefits from the subcooled boundary layer and may be expected to behave more like pool boiling; CHF would be precipitated in these regions.

4.2. Impinging jet flow disruption

The rising buoyant vapor bubbles are found to disrupt the impinging jet in addition to the horizontal velocities discussed in Section 4.1. At the lower heat inputs shown in Figure 5, (Bl^* = 0.45 and 0.69 for Re = 5,000; Bl^* = 0.33 and 0.53 for Re = 15,000), vapor bubbles are not yet widespread enough to completely obscure the impinging liquid flow from view and velocity measurements may still be obtained in this region. The average vertical velocity profiles of the impinging jet are presented in Figure 8 for different heat fluxes and at multiple vertical heights (z/d positions). The unheated (Bl^* = 0) single-phase case displays symmetric velocity profiles indicative of a developing jet. These impinging jet velocity profiles are in very good agreement with previous single-phase measurements for confined impinging jets formed by sharp-edged orifices (Fitzgerald and Garimella 1998). With an increase in the heat input and vapor generation, the vertical velocity profile of the impinging jet is altered. Increasing vapor generation attenuates the impinging jet flow as indicated by the reduced velocity profile magnitudes in Figure 8a for Re = 5,000 and Figure 8b for Re = 15,000. The impingement velocity modification at the higher heat inputs is not limited to regions close to the heat source, as reduced velocities can be observed in the profiles plotted farther from the impingement surface at z/d = 2 and z/d = 3.

Figure 9 shows the jet centerline velocity plotted against z/d. The decay rate of the jet centerline velocity prior to impingement is calculated by fitting a linear relationship to the velocity data between z/d = 1.5 and 2.5 as shown in Figure 9. This z/d range is centered in the confinement gap and is chosen to avoid regions affected by the impingement surface or completely obscured by vapor. The centerline velocity decay rate (C) plotted in Figure 10 increases with increasing heat input, indicating that the jet

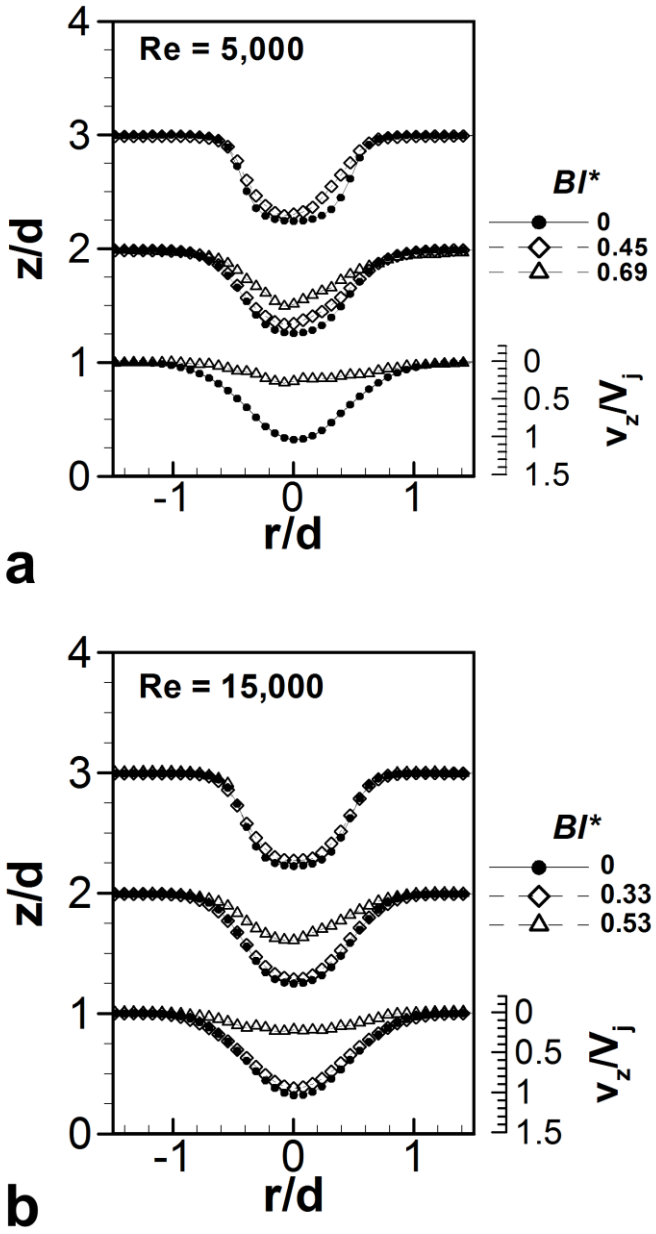

Figure 8. Vertical velocity profiles in the impinging jet at Reynolds numbers of (a) 5,000 and (b) 15,000 at various heat inputs.

decays more rapidly along its development length when vapor bubbles are present. This velocity decay occurs even with the higher momentum of the jet at a Reynolds number of 15,000, as shown in Figure 8-10. The higher Reynolds number jet initially shows very little increase in decay rate with heat input (*Bl**

= 0.33 in Figure 10), which is in contrast to the near-linear increase in decay rate with heat input displayed by the low Reynolds number jet. These results indicate that the higher momentum of the Re = 15,000 jet may initially overcome the flow resistance caused by the vapor bubbles in the flow.

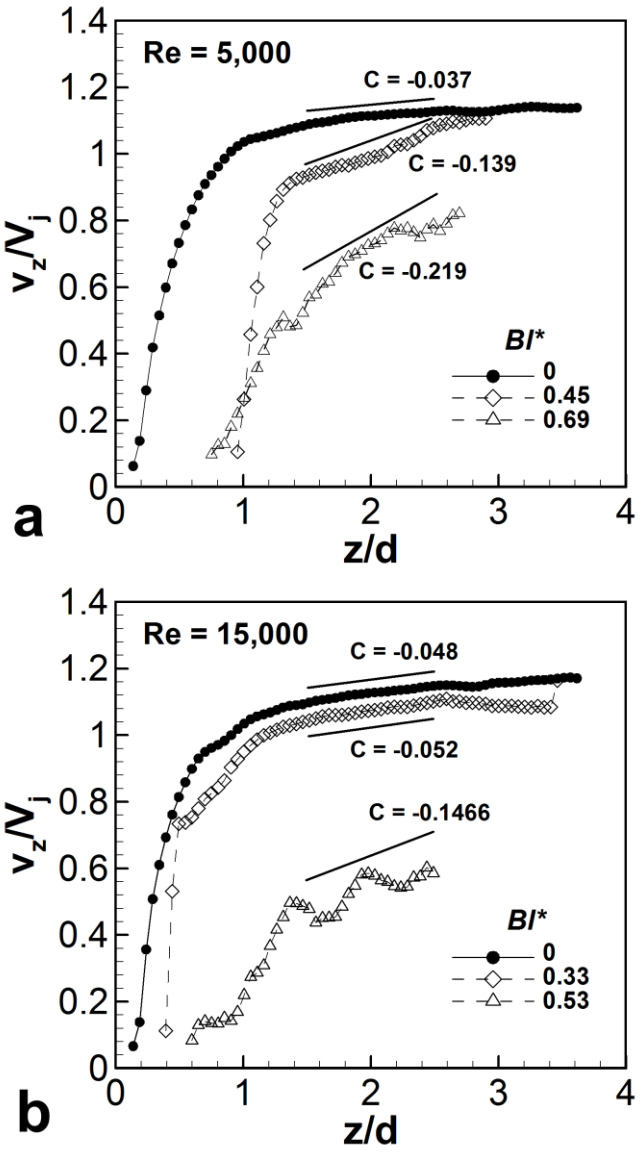

Figure 9. Jet centerline velocity for increasing heat inputs plotted against height from the impingement surface for the jet Reynolds number of (a) 5,000, and (b) 15,000.

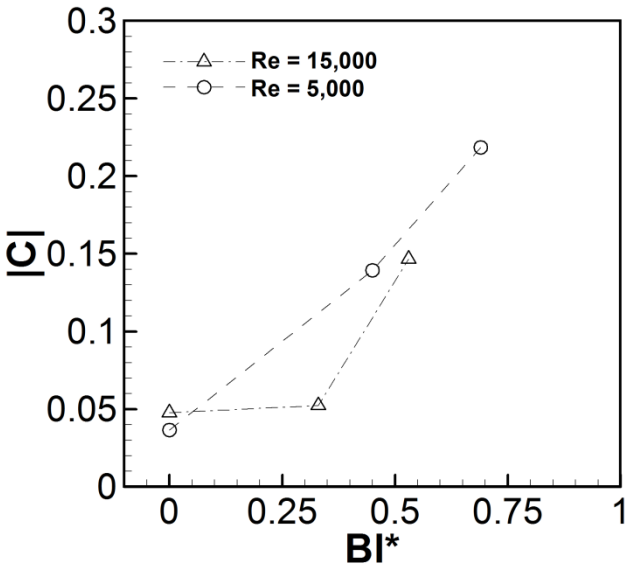

Figure 10. Decay rate of centerline jet velocity as a function of nondimensional heat input.

The impinging flow modification is significant in that the vapor bubbles from boiling dominate the impinging jet flow. This interaction of an impinging liquid flow with boiling has not yet been quantitatively demonstrated in the literature and has implications for two-phase impingement cooling system design and model development. The liquid flow conditions during boiling cannot be assumed identical to those during single-phase operation and the dependence of the impinging flow on the surrounding vapor must be considered.

4.3. Turbulence modulation

Profiles of turbulence intensity for each velocity component are shown in Figure 11 for Re = 5,000 and Figure 12 for Re = 15,000. The *y*-axis range is twice as large for the lower Reynolds number due to the higher relative bubble-generated turbulence. A range of heat inputs are shown to illustrate the evolution of velocity fluctuations with increasing vapor generation.

The horizontal ($v'_{r,rms}/V_j$) and vertical ($v'_{z,rms}/V_j$) single-phase turbulence intensity (respectively plotted in subfigure (i) and (ii) in Figure 11a and Figure 12a) show similar trends as have been presented

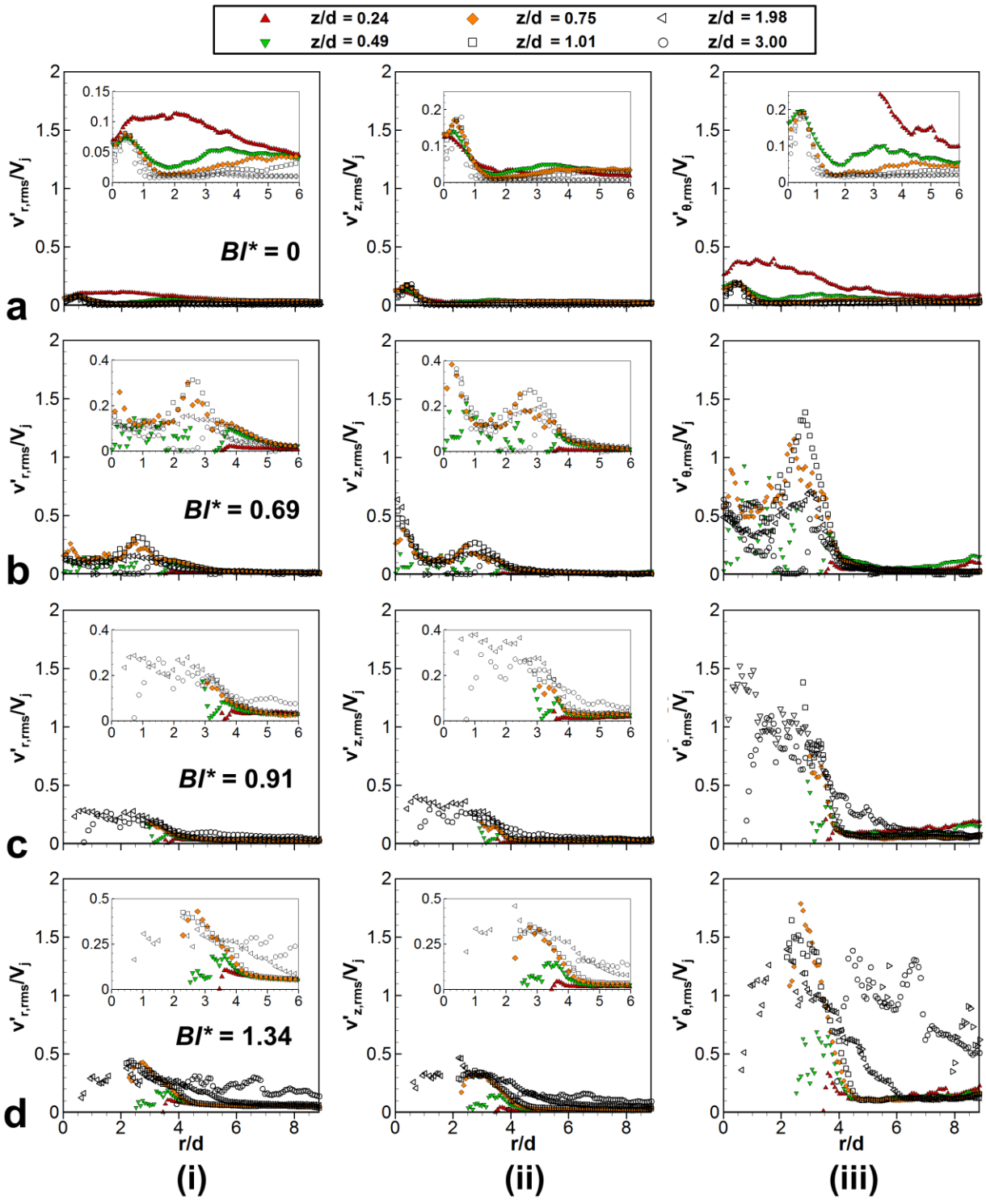

Figure 11. (a-d) Profiles of turbulence intensity for different heat inputs. Subfigures show (i) radial velocity component, (ii) vertical velocity component, and (iii) circumferential velocity component as a function of radial distance for the jet Reynolds number of 5,000.

in the literature for turbulence in confined impinging jets (Fitzgerald and Garimella 1998). At z/d positions greater than 0.24, a peak intensity at approximately $r/d = 0.5$ in both radial and axial components indicates a peak in turbulence at the edge of the impinging jet. The stereo-PIV measurements used in the present study uniquely allow calculation of the circumferential velocity in this axisymmetric geometry. This velocity component has not been previously reported for a confined impinging jet configuration, and is shown to be of similar or slightly higher magnitude compared to the radial and vertical velocity fluctuations (subfigure (iii) in Figure 11a and Figure 12a).

As the heat input is increased, the turbulence fluctuations are altered dramatically. At $Bl^* = 0.69$ for the Re = 5,000 jet (Figure 11b) and $Bl^* = 0.53$ for the Re = 15,000 jet (Figure 12b), a large increase in jet centerline axial velocity turbulence intensity is shown in subfigure (ii). This increase in turbulence intensity at the jet centerline is consistent with results for bubbly jets (Kumar *et al*. 1989), indicating that the increased turbulence in this region is likely caused by the small bubbles that are entrained into the jet from the surrounding flow field at this heat input. This increased turbulence intensity occurs at the same heat input that shows significant jet centerline velocity decay (Figure 9), indicating that vapor-bubble-induced velocity fluctuations are contributing to the decay of jet velocity. At $Bl^* = 0.69$ and Re = 5,000 there is also an increase in radial and circumferential turbulence at $r/d = 3$. The circular heat source extends to a radial position of 3.39 diameters; the location of the turbulence enhancement at this heat input is likely indicative of the turbulence created by bubble formation and departure close to the edge of the heat source. Turbulence enhancement at this location is also displayed in the higher Reynolds number case at $Bl^* = 0.53$ (Figure 12b).

Further increases in heat input (Figure 11c,d and Figure 12c,d) result in comparable magnitudes and distributions of vertical- and radial-component turbulence. In contrast, the circumferential component shows a turbulence intensity that is two- to three-times higher than the other directions. The circumferential turbulence intensity is largest at the edge of the heater (between $r/d = 3$ and 4), indicating that boiling close to the edge of the circular heat source is the cause of higher velocity fluctuations in the out-of-plane direction. Turbulence in the confinement gap downstream of the heat source ($r/d > 4$) is

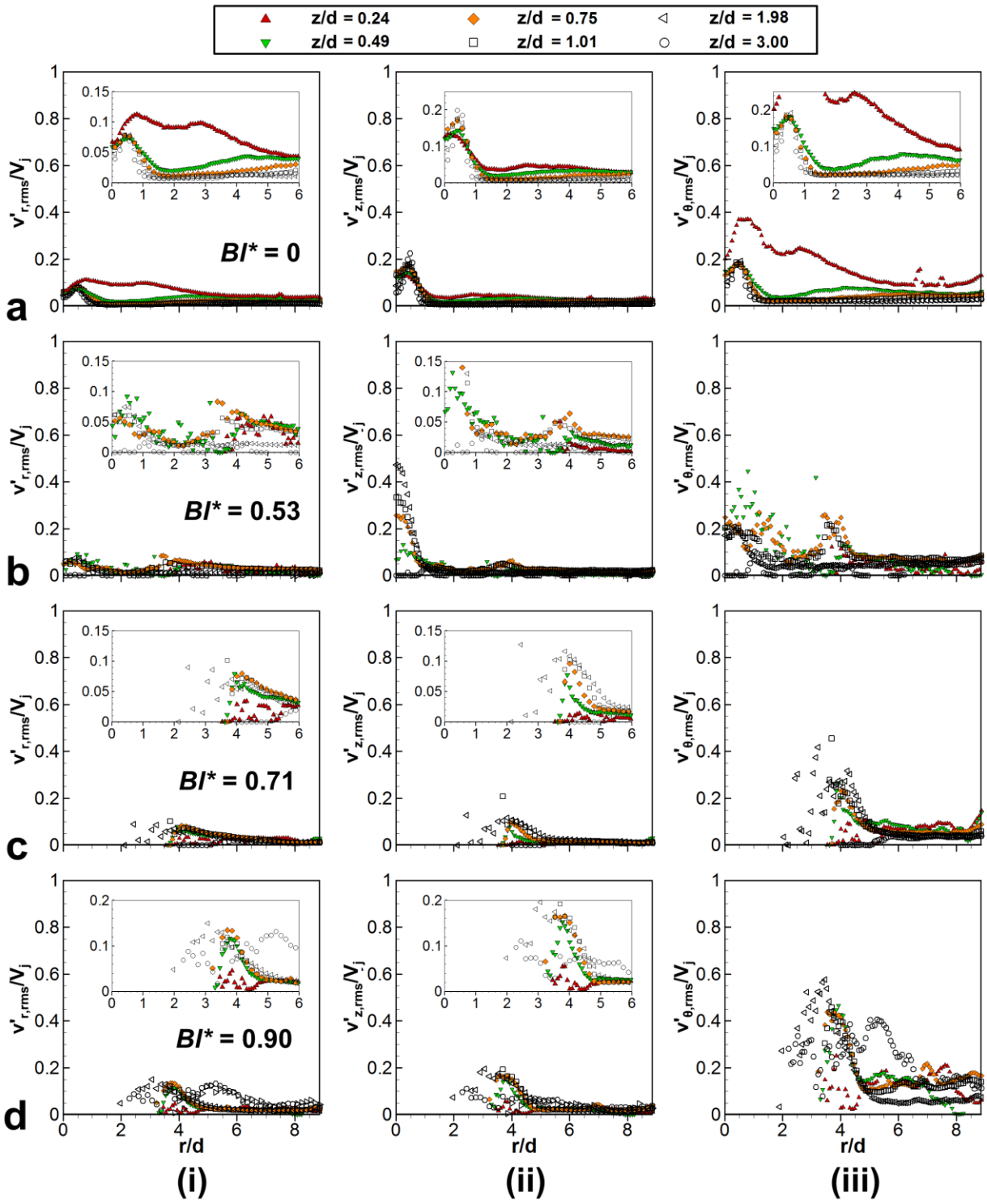

Figure 12. (a-d) Profiles of turbulence intensity for different heat inputs. Subfigures show (i) radial velocity component, (ii) vertical velocity component, and (iii) circumferential velocity component as a function of radial distance for the jet Reynolds number of 15,000.

minimal in all cases except the circumferential velocity component at the highest heat flux at each Reynolds number, shown in Figure 11d (iii) and Figure 12d (iii). The higher turbulence intensity in this region is notably displayed only at z/d = 1.98 and z/d = 3.00. Considering the flow patterns shown in Figure 6, this high turbulence intensity at higher z/d positions is likely caused by the bubble-generated turbulence being carried upwards and outwards due to the reverse liquid flow pattern indicative of the vapor-dominated flow regime at these heat inputs.

4.4. Turbulent kinetic energy exchange and dissipation

The turbulence intensities shown in Figure 11 and Figure 12 indicate an increase in turbulence caused by vapor generation. Gas bubbles in a turbulent liquid flow can both enhance turbulence and increase turbulence dissipation (Balachandar and Eaton 2010). Turbulence kinetic energy (*TKE*) is calculated from the fluctuating v_r-, v_z-, and v_θ-component velocities as

$$TKE = \frac{1}{2}\left(\overline{v_r'^2} + \overline{v_z'^2} + \overline{v_\theta'^2}\right). \tag{3}$$

The calculation of dissipation rate is less straightforward. Direct calculation of the dissipation rate requires the full three-dimensional velocity gradient tensor and measurement resolution on the order of the Kolmogorov scale of the flow (Tanaka and Eaton 2007), estimated at approximately 3 μm for the jet Reynolds number of 15,000 in the current experiments. PIV windowing is analogous to the filtering of the momentum equations used in Large-Eddy Simulations (LES); thus an LES approach can be used to estimate the dissipation rate of *TKE*. The dissipation rate (ε) is estimated using the Smagorinsky model, as outlined by Sheng *et al*. (2000), where

$$\varepsilon = \left(C_s\Delta\right)^2 \left\langle \overline{S}^3 \right\rangle, \tag{4}$$

and $\overline{S}$ is the filtered rate of strain. A filter size (Δ) corresponding to the average of the PIV window r and z dimensions (1.152 × 0.768 mm) is used with a Smagorinsky constant of C_s = 0.17.

Contour maps of *TKE* and dissipation rate are shown in Figure 13 for the jet at a Reynolds number of 5,000. White regions in these plots indicate areas with insufficient data samples. The single-phase jet (shown in Figure 13a) is characterized by strong *TKE* and dissipation rate in the jet shear layer at r/d = 0.5. The modification of turbulence within the impinging jet by bubbles from the boiling heat source is shown in Figure 13b for Bl^* = 0.69. *TKE* and dissipation rate are now highest at the center of the impinging jet and *TKE* produced by the bubbles departing the edge of the heat source ($r/d \approx 3$) is similar in magnitude to the *TKE* shown in the central jet regions.

At the heat input of Bl^* = 0.91 (shown in Figure 13c), the region of high *TKE* becomes more uniformly distributed across the channel height at $r/d \approx 3.5$. The distribution of *TKE* at Bl^* = 1.34 (Figure 13d) differs from the other operating conditions presented; the regions of high *TKE* extend radially downstream to the edge of the confinement gap. This heat input represents an operating point at which the bulk flow reaches saturated conditions ($Bl^* \geq 1$). Comparing the distribution of *TKE* shown in Figure 13d to those at subcooled exit conditions (Figure 13a-c), it is clear that turbulence is primarily contained to within the boiling region near the heat source ($r/d \leq 4$) when saturated conditions are not reached.

The trend of increasing *TKE* with increasing amounts of vapor discussed above is in agreement with the turbulence kinetic energy measurements in the literature for bubbly pipe flow. Lance and Bataille (1991) studied vertical air-water bubbly flow and found that bubbles were the dominant source of *TKE* at high void fractions. A similar dependence on void fraction has been observed by other researchers (Hibiki and Ishii 1999; Roy *et al.* 2002).

Dissipation rate is highest in the bubbly regions of the flow. This is particularly evident at Bl^* = 0.91 and Bl^* = 1.34 in Figure 13 where $r/d < 3$ (*i.e.*, directly above the boiling heat source). Bubble drag can act to increase dissipation (Balachandar and Eaton 2010), which would have the largest effect in this region where bubble departure and rise due to buoyancy is the greatest. Additionally, bubble interfaces can act to oppose turbulence fluctuations; the deformable liquid-vapor interface can act to absorb *TKE* and increase the dissipation rate (Wang *et al.* 1987; Serizawa and Kataoka 1990).

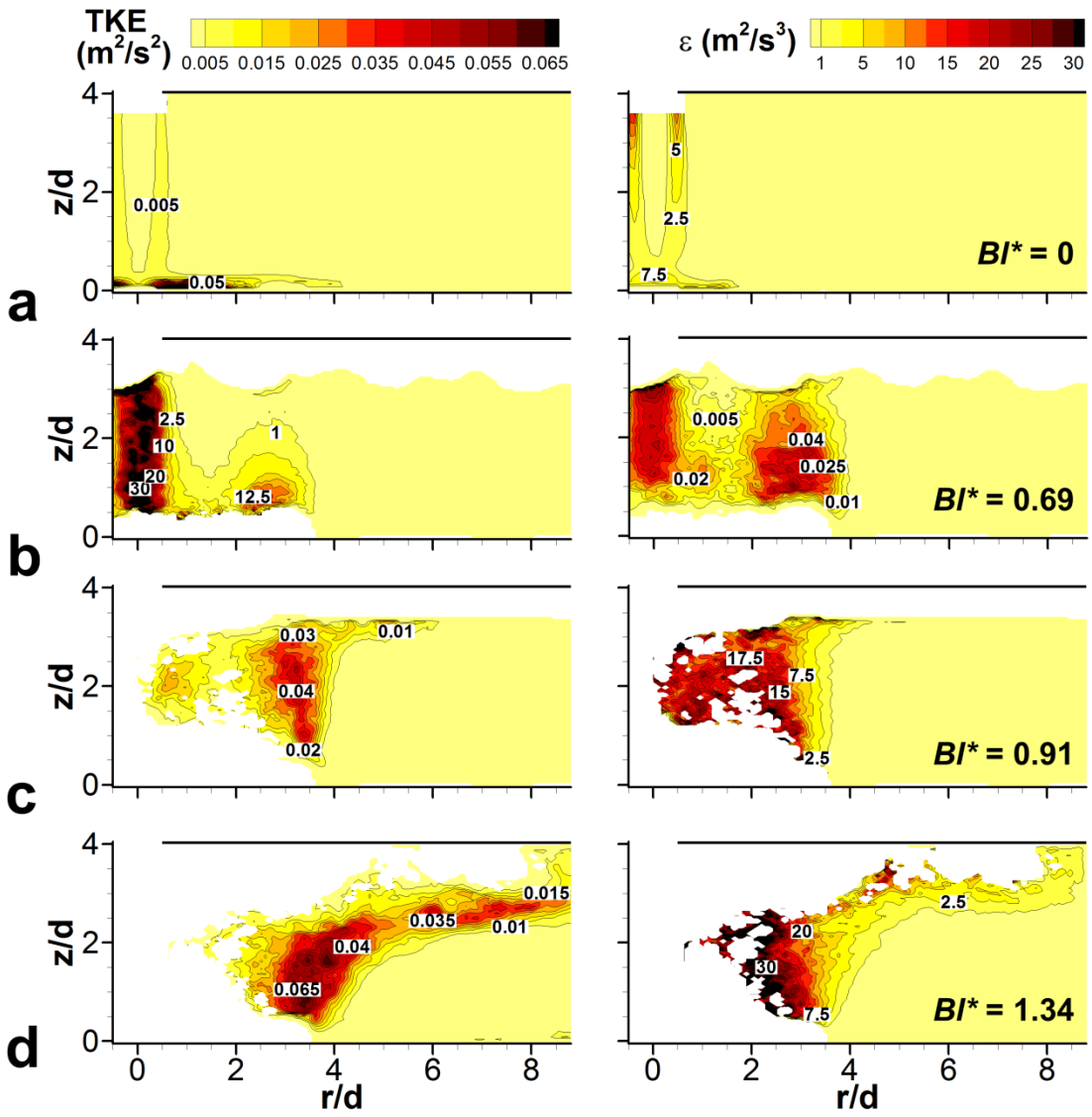

Figure 13. Turbulent kinetic energy (left) and dissipation rate (right) at various heat inputs for the jet at a Reynolds number of 5,000.

The link between turbulence and vapor bubbles is further investigated by considering the spectra of *TKE*. Figure 13b shows that the regions of highest *TKE* occur within the jet when vapor bubbles are present (shown at $Bl^* = 0.69$). A similar result is also found at the jet Reynolds number of 15,000. Spectra of normalized *TKE* ($TKE^* = TKE/V_{jet}^2$) are calculated along the jet centerline ($r/d = 0$) at the center of the confinement gap ($z/d = 2$) at heat inputs of $Bl^* = 0.69$ and 0.53 for the jet Reynolds numbers of 5,000 and 15,000, respectively. Also plotted is the power spectrum of the vapor presence (PSD_v) at the

same location, taken as the continuous on-off signal provided by the dynamic mask. Spectra are calculated using the Lomb-Scargle method, which accommodates the gappy data sampling inherent in two-phase regions.

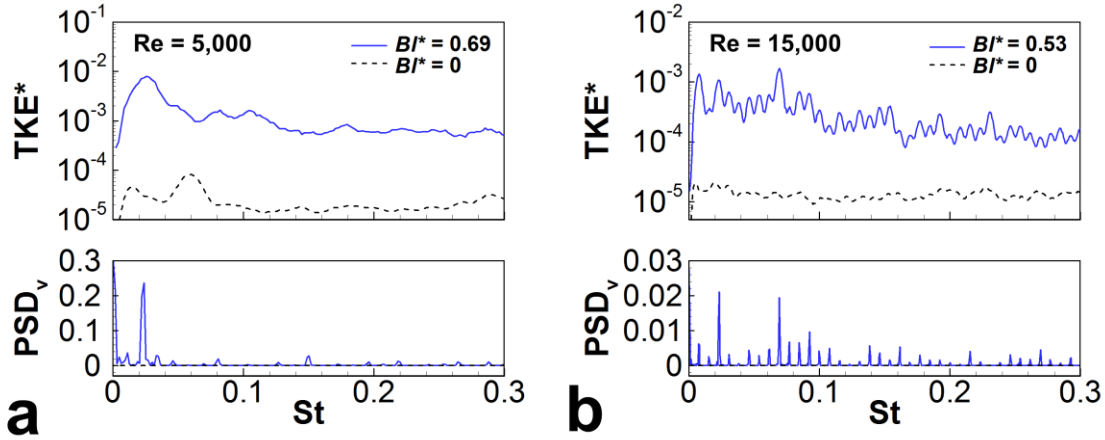

Figure 14. Normalized turbulence kinetic energy spectra plotted with power spectra of the vapor mask for (a) Re = 5,000, and (b) Re = 5,000. The spectra are calculated along the jet centerline (r/d = 0) at the midpoint in the confinement gap (z/d = 2).

Figure 14a shows a peak in *TKE* at a Strouhal number (St = fd/V_{jet}) of 0.023, which agrees very well with the peak frequency in the power spectrum of vapor at this Reynolds number. No peak at this Strouhal number is observed at *Bl** = 0, indicating that the periodic presence of vapor bubbles in the jet flow is the primary cause of the elevated *TKE* values in the jet. At the jet Reynolds number of 15,000 (Figure 14b), the vapor signal shows many additional frequency peaks, which also translate into peaks in the *TKE* spectrum. The higher Reynolds number likely causes more complex liquid-bubble interactions that result in the wider distribution of peak frequencies compared to the Reynolds number of 5,000. Interestingly, the strongest peak frequency in vapor signal at the Reynolds number of 15,000 is also St = 0.023, indicating that this Strouhal number may be important in the dynamic interaction of gas bubbles and jet flows and that the scaling of frequency with the jet diameter and velocity is appropriate.

Conclusions

The turbulent flow field in confined jet impingement with boiling is investigated at jet Reynolds numbers of 5,000 and 15,000 across a range of heat inputs. The modification of the flow field and turbulence due to vapor generation from boiling is quantified and reported.

Boiling greatly modifies the liquid velocities and flow structure within the confinement gap. Vapor bubbles disrupt both the impinging jet and wall jet flow; vapor generation results in lower liquid jet velocities compared to single-phase cases. The impinging jet is disrupted by the rising vapor bubbles, resulting in a breakdown of the traditional impinging jet flow structure and causing instead a more uniform velocity profile across the confinement-gap height. As heat input and vapor generation increase, a vapor plume structure surrounding the heat source is found to dominate the flow field within the confinement gap even at the higher jet Reynolds number of 15,000. Large rising vapor bubbles drive the liquid flow recirculation in the opposite direction compared to that of the single-phase case.

Vapor generation is a significant source of turbulence production and dissipation in the flow. Turbulence production is high in regions adjacent to where bubbles grow and depart. The effect of the bubbles on turbulence intensity in the flow is relatively lower for the higher Reynolds number jet. When subcooled exit conditions are maintained, the turbulence kinetic energy exchange is primarily limited to the regions near the heated surface within the confinement gap. Saturated exit conditions are found to be necessary to cause bubble-induced *TKE* production or dissipation downstream towards the confinement-gap edge. The dissipation rate is shown to be highest within the bubbly regions directly above the heated surface. Within the impinging jet, turbulence spectra show that the primary frequencies of turbulence in the impinging jet are directly linked to bubble induced fluctuations. A Strouhal number of 0.023 is identified to be potentially important in the dynamic interaction of bubbles with liquid jets.

This study presents the first turbulence flow measurements within subcooled confined jet impingement boiling. The results indicate that boiling has a large influence on the liquid velocities and turbulence within both the impinging jet and liquid in the confinement gap. The results presented have direct implications on the effective design of cooling devices based on confined jet impingement. Models

and correlations to predict the cooling capabilities of confined two-phase jet impingement must include the bubble-induced flow modifications, as boiling contributions to the cooling performance of two-phase jet impingement cannot be simply superimposed on the single-phase convective contributions of the impinging jet.

References

ANSYS® FLUENT, Academic Research, Release 15.0.

Balachandar, S., Eaton, J.K., 2010. Turbulent dispersed multiphase flow, Annu. Rev. Fluid Mech. 42, 111-133.

Bradshaw, P., Love, E.M., 1959. The normal impingement of a circular air jet on a flat surface. Aeronaut. Res. Counc. R & M 3205.

Cornaro, C., Fleischer, A.S., Goldstein, R.J., 1999. Flow visualization of a round jet impinging on cylindrical surface, Exp. Therm. Fluid Sci. 20, 66-78.

Donaldson, C.D., Snedeker, R.S., Margolis, D.P., 1971. A study of free jet impingement. Part 2. Free jet turbulent structure and impingement heat transfer. J. Fluid Mech. 45, 477-512.

Eckstein, A.C., Charonko, J., Vlachos, P., 2008. Phase correlation processing for DPIV measurements. Exp. Fluids 45, 485-500.

Eckstein, A., Vlachos, P.P., 2009a. Assessment of advanced windowing techniques for digital particle image velocimetry (DPIV), Meas. Sci. Technol. 20, 075402.

Eckstein, A., Vlachos, P.P., 2009b. Digital particle image velocimetry (DPIV) robust phase correlation, Meas. Sci. Technol. 20, 055401.

Estrada-Perez, C.E., Hassan, Y.A., 2010. PTV experiments of subcooled boiling flow through a vertical rectangular channel, Int. J. Multiphase Flow 36, 691-706.

Fitzgerald, J.A., Garimella, S.V., 1997. Flow field effects on heat transfer in confined jet impingement, J. Heat Transf. 119, 630-632.

Fitzgerald, J.A., Garimella, S.V., 1998. A study of the flow field of a confined and submerged impinging jet, Int. J. Heat Mass Tran. 41, 1025-1034.

Garimella, S.V., 2000. Heat transfer and flow fields in confined jet impingement, Ann. Rev. Heat Transfer 11, 413-494.

Hassan, Y.A., Blanchat, T.K., Seeley, C.H., Canaan, R.E., 1992. Simultaneous velocity measurements of both components of a two-phase flow using particle image velocimetry, Int. J. Multiphase Flow 18, 371-395.

Hassan, Y.A., Estrada-Perez, C.E., Yoo, J.S., 2014. Measurement of subcooled flow boiling using particle tracking velocimetry and infrared thermographic technique, Nucl. Eng. Des. 268, 185-190.

Hibiki, T., Ishii, M., 1999, Experimental study on interfacial area transport in bubbly two-phase flows, Int. J. Heat Mass Tran. 42, 3019-3035.

Hussein, H.J., Capp, S.P., George, W.K., 1994. Velocity measurements in a high-Reynolds-number momentum-conserving, axisymmetric, turbulent jet, J. Fluid Mech. 258, 31-75.

Khalitov, D.A., Longmire, E.K., 2002. Simultaneous two-phase PIV by two-parameter phase discrimination, Exp. Fluids, 32, 252-268.

Kumar, S., Nikitopoulos, D.N., Michaelides, E.E., 1989, Effect of bubbles on the turbulence near the exit of a liquid jet, Exp. Fluids 7, 487-494.

Lance, M., Bataille, J., 1991. Turbulence in the liquid phase of a uniform bubbly air-water flow, J. Fluid Mech. 222, 95-118.

Lindken, R., Merzkirch, W., 2002. A novel PIV technique for measurements in multiphase flows and its application to two-phase bubbly flows, Exp. Fluids 33, 814-825.

Liu, Z., Zheng, Y., Jia, L., Zhang, Q., 2005. Study of bubble induced flow structure using PIV, Chem. Eng. Sci. 60, 3537-3552.

Martin, H., 1977. Heat and mass transfer between impinging gas jets and solid surfaces, Adv. Heat Transfer 13, 1-60.

Morris, G.K., Garimella, S.V., 1998. Orifice and Impingement Flow Fields in Confined Jet Impingement, J. Heat Transf. 120, 68-72.

Popiel, C.O., Trass, O., 1991. Visualization of a free and impinging round jet, Exp. Therm. Fluid Sci. 4, 253-264.

Prasad, A.K., Jensen, K., 1995. Scheimpflug stereocamera for particle image velocimetry in liquid flows, Appl. Optics 34, 7093-7099.

Qiu, L., Dubey, S., Choo, F.H., Duan, F., 2015. Recent developments of jet impingement nucleate boiling, Int. J. Heat Mass Tran. 89, 42-58.

Rau, M.J., Garimella, S.V., 2013. Local two-phase heat transfer from arrays of confined and submerged impinging jets. Int. J. Heat Mass Tran. 67, 487-498.

Rau, M.J., Garimella, S.V., 2014. Confined jet impingement with boiling on a variety of enhanced surfaces. J. Heat Transf. 136, 101503.

Rau, M.J., Garimella, S.V., Dede, E.M., Joshi, S.N., 2015. Boiling heat transfer from an array of round jets with hybrid surface enhancements. J. Heat Transf. 137, 071501.

Roy, R.P., Hasan, A., Kalra, S.P., 1993. Temperature and velocity fields in turbulent liquid flow adjacent to a bubbly boiling layer, Int. J. Multiphase Flow 19, 765-795.

Roy, R.P., Kang, S., Zarate, J.A., 2002. Turbulent subcooled boiling flow – experiments and simulations, J. Heat Transf. 124, 73-93.

Roy, R.P., Velidandla, V., Kalra, S.P., 1997. Velocity field in turbulent subcooled boiling flow, J. Heat Transf. 119, 754-766.

Serizawa, A., Kataoka, I., 1990. Turbulence suppression in bubbly two-phase flow, Nucl. Eng. Des. 122, 1-16.

Sheng, J., Meng, H., Fox, R.O., 2000. A large eddy PIV method for turbulence dissipation rate estimation, Chem. Eng. Sci. 55, 4423-4434.

So, S., Morikita, H., Takagi, S., Matsumoto, Y., 2002. Laser Doppler velocimetry measurement of turbulent bubbly channel flow, Exp. Fluids 33, 135-142.

Soloff, S.M., Adrian, R.J., Liu, Z.-C., 1997. Distortion compensation for generalized stereoscopic particle image velocimetry, Meas. Sci. Tecnol. 8, 1441-1454.

Tanaka, T., Eaton, J.K., 2007. A correction method for measuring turbulence kinetic energy dissipation rate by PIV, Exp. Fluids 42, 893-902.

Vader, D.T., Incropera, F.P., Viskanta, R., 1992. Convective nucleate boiling on a heated surface cooled by an impinging, planar jet of water, J. Heat Transf. 114, 152-160.

Wang, S.K., Lee, S.J., Jones, O.C., Lahey, R.T., 1987. 3-D turbulence structure and phase distribution measurements in bubbly two-phase flows, Int. J. Multiphas. Flow 13, 327-343.

Westerweel, J., Scarano, F., 2005, Universal outlier detection for PIV data, Exp. Fluids 39, 1096-1100.

Wieneke, B., 2005. Stereo-PIV using self-calibration on particle images, Exp. Fluids 39, 267-280.

Wolf, D.H., Incropera, F.P., Viskanta, V., 1993. Jet impingement boiling, Adv. Heat Transfer 23, 1-132.

Xiong, G., Zhou, X., Ji, L., 2006, Automated segmentation of drosophila RNAi fluorescence cellular images using deformable models, IEEE T. Circuits-I 53, 2415-2424.

Xue, Z., Charonko, J.J., Vlachos, P.P., 2015. Particle image pattern mutual information and uncertainty estimation for particle image velocimetry, Meas. Sci. Technol. 26, 074001.

.

List of Figures

Figure 14. Normalized turbulence kinetic energy spectra plotted with power spectra *of* the vapor mask for (a) Re = 5,000, and (b) Re = 5,000. The spectra are calculated along the jet centerline ($r/d = 0$) at *the midpoint* in the confinement gap ($z/d = 2$).